C. T. Johansen · C. D. McRae · P. M. Danehy · E. C. A. Gallo · L. M. L. Cantu · G. Magnotti · A. D. Cutler · R. D. Rockwell, Jr. · C. P. Goyne · J. C. McDaniel

OH PLIF Visualization of the UVa Supersonic Combustion Experiment: Configuration A

Abstract Hydroxyl radical (OH) planar laser-induced fluorescence (PLIF) measurements were performed in the University of Virginia supersonic combustion experiment. The test section was set up in configuration A, which includes a Mach 2 nozzle, combustor, and extender section. Hydrogen fuel was injected through an unswept compression ramp at two different equivalence ratios. Through the translation of the optical system and the use of two separate camera views, the entire optically accessible range of the combustor was imaged. Single-shot, average, and standard deviation images of the OH PLIF signal are presented at several streamwise locations. The results show the development of a highly turbulent flame structure and provide an experimental database to be used for numerical model assessment.

1 Introduction

The main motivators for developing scramjet engines are to realize high speed, long distance transport, improve missile efficiency, and to reduce the cost of placing payloads into orbit. The inherent advantage of scramjets over conventional rocket engines is the ability to use atmospheric oxygen instead of carrying an onboard oxidizer. This results in an increase in the engine's specific impulse over a wide range of Mach (Ma) numbers (Fry 2004). A recent analytical study by Tetlow and Doolan (2007) shows that, for a given payload mass, a hydrogen- or hydrocarbon-fueled scramjet stage uses significantly less fuel than a fully rocket-powered stage for orbital insertion. They also show, however, that to be economically viable, the scramjet stage must be reusable since it has more structural mass than an equivalent fully rocket-powered system. This requires a robust design, a long operating life, and an easily recoverable system. A logical solution is to integrate the engine with a lifting vehicle airframe.

Although recent scientific flight experiments (Smart et al. 2006; Smart 2009) and demonstration projects (Voland et al. 2006; Hank et al. 2008) have shown that scramjets are feasible in principle, many technical hurdles still remain. One significant hurdle is that the engine is unable to operate over the complete range of flight conditions ($0 < Ma < 25$) needed to achieve orbital insertion (Heiser and Pratt 1994). Scramjets rely on aerodynamic compression through a series of oblique shock waves and can only operate over a limited Mach number range ($5 < Ma < 15$) (Curran 2001; Forescue and Stark 1995). Through normal-shock compression and combustion at subsonic speeds, ramjets provide thrust at high specific impulses and over lower Mach number ranges (e.g. $3 < Ma < 6$ for a

Craig T. Johansen, Colin D. McRae
University of Calgary, Calgary, AB, Canada
E-mail: johansen@ucalgary.ca
Tel.: +1-403-220-7421

Paul M. Danehy
NASA Langley Research Center, Hampton, VA, USA

Emanuela C.A. Gallo, Luca M.L. Cantu, Gaetano Magnotti, Andrew D. Cutler
The George Washington University, Newport News, VA, USA

Robert D. Rockwell, Jr., Chris P. Goyne, James C. McDaniel
University of Virginia, Charlottesville, VA, USA

hydrogen-fueled ramjet) (Fry 2004). Similar to scramjets, ramjets have few to no moving parts, resulting in a relatively simple design for manufacture and reliability.

The integration of a ramjet and a scramjet into a single engine is referred to as a dual-mode scramjet. In this type of engine both subsonic and supersonic modes of combustion are possible, which extends the total operating Mach number range. With improvements in computer processing power, it is becoming more feasible to design and optimize these engines using computational fluid dynamics (CFD). Unfortunately, the flowfield associated with a dual-mode scramjet engine is difficult to predict. The flow includes non-linear interactions between turbulence and combustion, dynamic movement of shock waves, mixed regions of subsonic/supersonic flow, flow separation, fuel-air mixing, transition to turbulence, chemistry, and real gas effects. Even in the scramjet mode, there are regions of subsonic flow near the wall and the injector that interact with supersonic flow in the core (Fry 2004). In addition, the engine geometry, including the isolator length, plays a large role in determining the type of flow that enters the combustor (Heiser and Pratt 1994). Only through experimental validation can numerical modeling be trusted to accurately predict this type of flow.

Model validation is a significant objective of the University of Virginia's (UVa) continuous flow, dual-mode Supersonic Combustion Facility (UVaSCF). This facility operates as part of the National Center for Hypersonic Combined-Cycle Propulsion (NCHCCP) program, funded by the Air Force Office of Scientific Research (AFOSR) and NASA. The UVaSCF accommodates several flow configurations and can replicate conditions representative of both ramjet and scramjet modes of combustion. Using a series of non-intrusive diagnostics, large amounts of both qualitative and quantitative information can be acquired without perturbing the flow. Through an overlap in the types of data extracted from the different techniques there is redundancy in the data set which is important for credibility. The redundancy also offers information needed to determine the limits of some of the techniques. Measurements using focused schlieren (Rockwell et al. 2012), stereoscopic particle image velocimetry (SPIV) (Rockwell et al. 2012), tunable diode laser absorption spectroscopy (TDLAS) (Goldstein et al. 2011), tunable diode laser absorption tomography (TDLAT) (Busa et al. 2011), coherent anti-Stokes Raman spectroscopy (CARS) (Cutler et al 2012), and hydroxyl radical (OH) planar laser induced fluorescence (PLIF) (Johansen et al. 2012) are in the process of being performed in this facility.

The OH PLIF measurements in the combustor section of configuration A are reported herein. The two primary objectives are to produce a high quality experimental dataset for model assessment and to learn more about the physics of the flow through the interpretation of the PLIF images. The position of the PLIF measurement plane and the equivalence ratio were varied for completeness and to provide more than one condition for comparison.

2 UVa Dual-Mode Scramjet Facility

The UVaSCF is a vertically oriented, continuous running, direct-connect scramjet facility. The modular nature of the facility allows it to be assembled in various configurations. In the current study, configuration A was selected, shown on the right in Fig. 1. A schematic of the facility, shown on the left in Fig. 1, displays a large electrically heated air supply, test section, and exhaust system. Because the exhaust system is not connected directly to the test section, exhaust is vented from the extender to atmospheric pressure. The electrical resistance heater ensures that no vitiated gas or other contaminants enter the freestream flow before entering the test section. The stagnation pressure and temperature are roughly 300 kPa and 1200 K, respectively.

A Mach 2 nozzle is used to accelerate the flow through the test section while enthalpy conditions correspond to flight at Mach 5 (Cutler et al 2012). The complete test section (only a subset of which is used herein) includes four modules: an isolator, a combustor, a TDLAT section, and an extender. Figure 2 shows a three dimensional rendering of each of the modules and the locations of the various diagnostic locations for configuration A. Note that the test section has been re-oriented horizontally in this figure. A constant area isolator section allows a shock train to stabilize ahead of the combustor section. The module has optical access to perform SPIV, CARS, and TDLAS measurements. The combustor section includes a single, unswept, wall-mounted compression ramp with a fuel injector. The compression ramp is characterized by a width of $W = 12.7$ mm, height of $H = 6.35$ mm, and the ramp surface is oriented at 10 degrees relative to the divergent wall of the combustor. The injector is positioned on the downstream side of the ramp and includes a converging-diverging conical nozzle to accelerate the hydrogen fuel to Mach 1.7 (Goyne et al. 2006). By controlling the mass flow rate of the fuel, the equivalence ratio (ϕ) was varied in the experiments from 0.18 to 0.36, with most of the data obtained at these two extremes. The equivalence ratio is defined as the mixture fuel-to-oxidizer ratio normalized by the stoichiometric fuel-to-oxidizer ratio. The centerline fuel jet direction is oriented approximately 7.1 degrees relative to the freestream flow. The combustor wall diverges from the opposing wall at an angle of 2.9 degrees starting from the leading edge of the compression ramp. To allow

for TDLAT measurements, a constant area section can be connected to the exit of the combustor. Finally, an expanding extender section completes the test section with a divergence angle of 2.9 degrees.
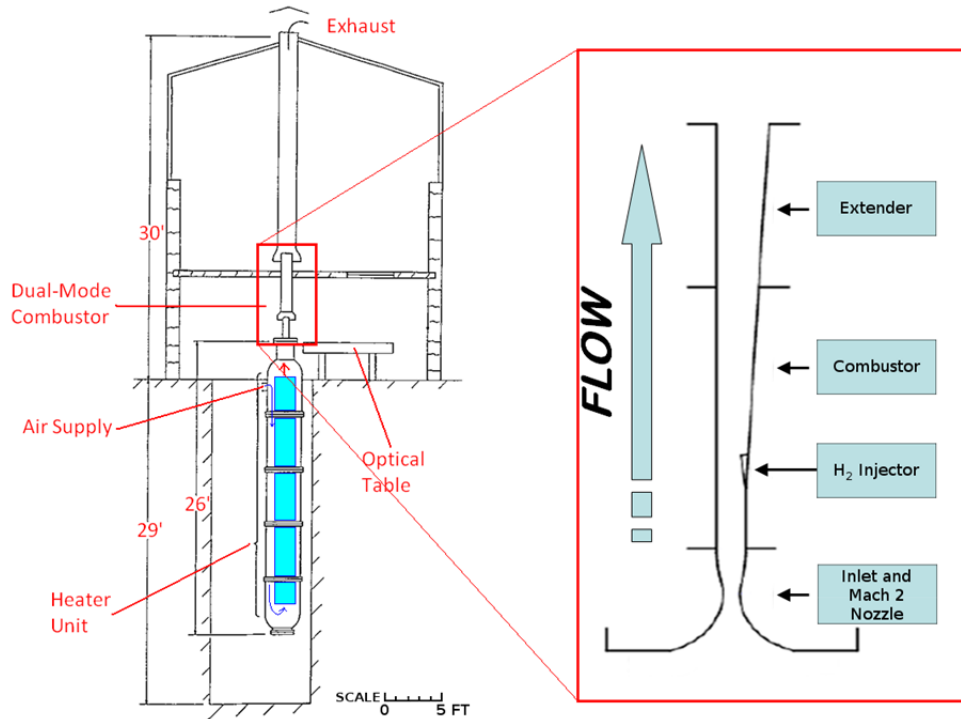

Fig. 1 UVaSCF facility. Configuration A displayed on right
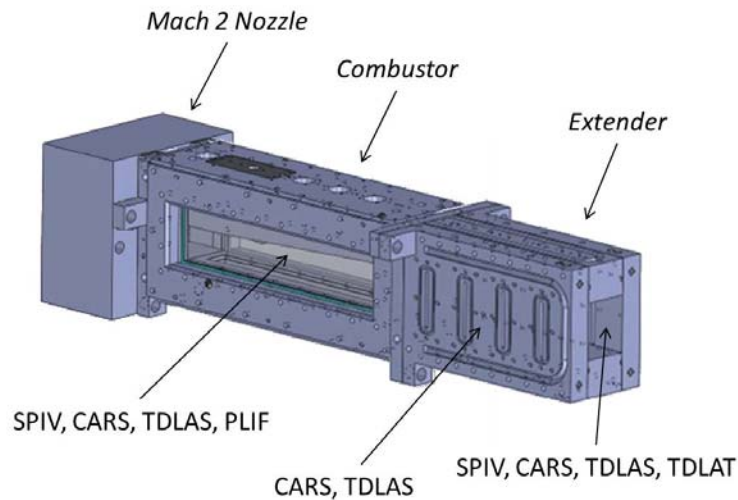

Fig. 2 Test section modules and diagnostic locations for configuration A. OH PLIF measurements in combustor section of configuration A are reported in current study

3 PLIF System Setup

To facilitate OH PLIF in the combustor section, ultraviolet (UV) grade fused silica windows were used for the side walls. This allowed for the transmission of the UV laser light from the laser source needed to excite the OH molecules and transmission of the subsequent fluorescence to the camera. An injection seeded, pulsed Nd:YAG was frequency doubled to 532 nm to pump a Spectra Physics PDL-2 dye laser, outputting tunable light at 567.1 nm. The

output of the dye laser was frequency doubled using a component of a wavelength extender (WEX) module to produce UV light at 283.55 nm. A HighFinesse WS-6 wavemeter was used to monitor the laser wavelength. At this wavelength the $Q_1(8)$ transition of OH was excited. This transition was selected because the PLIF signal is relatively insensitive to temperature, as reported by O'Byrne et al. (2005) in their OH PLIF measurements of a supersonic combustor using cavity injection in the T3 free-piston shock tunnel. The Nd:YAG and the dye laser were located on a mobile cart originally used as part of a CARS setup (Cutler et al 2012), which was later modified to include the doubling crystal from a WEX unit and associated beam separation and relay optics necessary for OH PLIF. Note that the laser operated at 20Hz but the CCD cameras framed at 10Hz, since the PI-MAX2 camera could not acquire full resolution images at greater than 13 Hz.
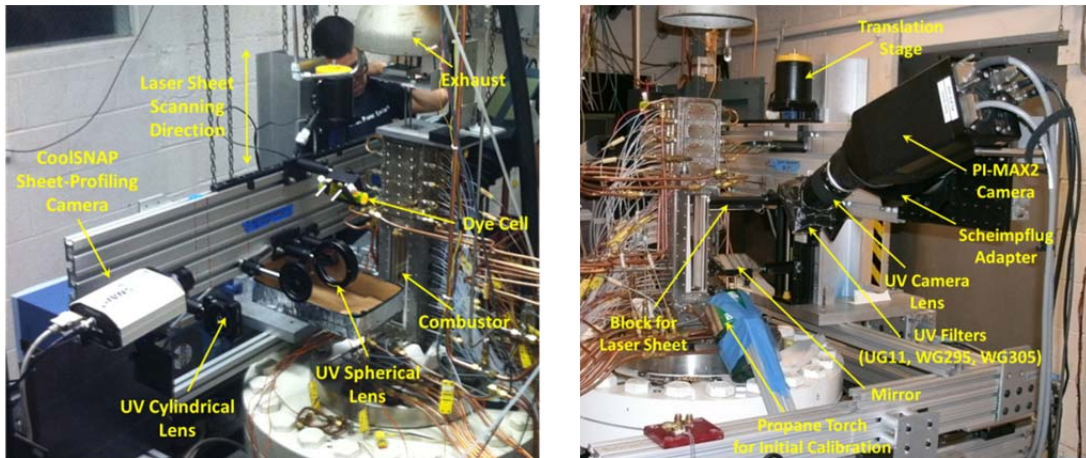

Fig. 3 Sheet forming optics and sheet profiling camera (left); and ICCD camera (right)

As shown in Fig. 3 (left), sheet forming optics, a dye cell, and a CoolSNAP sheet-profiling camera were mounted on a motorized vertical translation stage that was secured to a large optical table adjacent to the test section. A series of UV mirrors relayed the beam from the mobile laser cart onto the translation stage. The beam was expanded in one direction with a UV cylindrical lens (f=25mm) and then collimated with a UV spherical lens (50mm diameter, f=250mm). This produced a 50 mm wide and less than 1 mm thick laser sheet that was directed into the combustor, perpendicular to the flow axis. A beam splitter was placed between the test section and spherical lens to redirect part of the sheet up towards a Rhodamine dye filled quartz cell. Synchronized to the laser pulse, the unintensified CoolSNAP camera imaged the dye cell to measure any spatial non-uniformity in the laser sheet on a shot-by-shot basis. Spatial non-uniformity affects the PLIF signal since fluorescence is proportional to the excitation energy in the linear regime. The sheet profiling information was later used to correct the PLIF images.

The right image in Fig. 3 shows a PI-MAX2 ICCD (intensified charge-coupled device) camera with a UV Nikkor F/4.5 105 mm focal length lens that was used to image the PLIF signal. A beam block was placed at the laser sheet level to protect the camera. Schott UG11 (2mm), WG295 (2mm+1mm), and WG305 (2mm) filters were used to reduce laser scatter off the facility windows and combustor wall surfaces. A propane torch was used as a source of OH for initial calibration to optimize the laser's wavelength and help focus the PI-MAX2 camera. In addition to a streamwise traverse of the equipment, the laser sheet, mirrors and camera could translate approximately 10 inches in the horizontal direction, allowing a propane torch, dotcards, and imaging cards to be placed in the measurement plane without re-alignment of the equipment. A mirror was placed near the combustor window to allow the camera to image a more perpendicular view of the sheet than would have been otherwise possible with a direct camera view. A Scheimpflug adapter was used to help focus the camera on the image plane. Translating the sheet-forming optics, mirrors, and cameras along the flow axis allowed for a range of streamwise positions in the flow to be investigated.

The analysis of OH PLIF results herein are non-dimensionalized relative to the compression ramp height, H, with an emphasis on measurement planes at $x/H = 6$, 12, and 18 downstream of the injector plane. These measurement planes coincide with CARS measurements also taken with this test section configuration (Cutler et al 2012). Unfortunately, geometric constraints near the test section forced two different camera view configurations to be used to access the full range in the streamwise direction (Fig. 4). The first camera view (left) used one mirror and captured images from an upstream position. This view allowed imaging up to the downstream edge of the combustor window ($x/H = 23.5$). However, because the mirror was located near the facility nozzle, the entire system could only be translated up to a position of $x/H = 10.2$. In the second camera view (right), a pair of mirrors, one of which was

positioned further downstream, allowed the camera to image the PLIF signal from a downstream position. This extended the range of images to the upstream edge of the combustor window (x/H = -3.0). With this setup the laser sheet was able to translate upstream of the fuel injector. Because the camera imaged the PLIF signal from the opposite side of the laser sheet relative to camera view 1, the additional reflection from the second mirror was naturally corrected. As such, the PLIF in both views was captured from a perspective as though looking upstream with the laser-sheet coming in from the right. The images were later corrected in post-processing to match results from previous studies (Cutler et al. 2012; Fulton et al. 2012), such that the laser sheet would enter from the left.
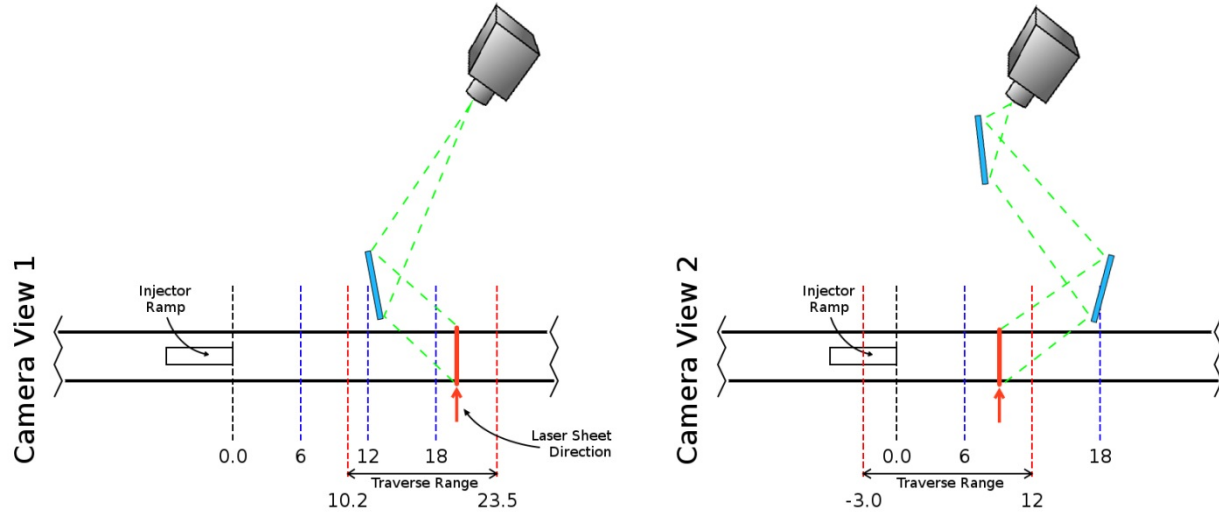

Fig. 4   Camera view 1 (left) and camera view 2 (right). Dimensions are displayed in x/H units

4 Post Processing

Optical distortions and distortions due to the camera perspective were corrected through post processing of the PLIF data. The process loosely follows the procedure outlined by Danehy et al. (2008) for nitric oxide (NO) PLIF. The post processing involved five major steps: dotcard analysis, unwarping of PLIF data, calibration sheet analysis, creation of correction sheets, and applying final corrections. The dotcard is a rectangular grid of uniform square dots with 3.175 mm (0.125-inch) spacing printed on white card stock. Given computer generated template dotcards and experimentally captured distorted dotcard images, the optical distortion was corrected using a plug-in for ImageJ (Rasband 2009), a freeware image processing software developed at the National Institutes of Health. The plug-in, a modification of UnwarpJ (Sorzano 2005) for working with image stacks, was used to apply the unwarping algorithm across each set of PLIF data to correct for the camera distortions. Note that the terminology "unwarp" is used herein to describe the process of using UnwarpJ to correct perspective and lens distortions of the PLIF images.

As described previously, two separate camera views were used to access the full streamwise range in the combustor, which was only limited by the length of the windows. In camera view 1, the angle of the Scheimpflug adapter was adjusted to optimize the picture quality. The Scheimpflug adapter was not adjusted after the switch between camera views because of time constraints in using the facility. In addition, camera view 2 had more perspective distortion, resulting in a lower y-pixel magnification. As a result, lower quality images were acquired using the camera view 2 configuration compared to images from camera view 1.

Figure 5 shows a sample single-shot PLIF image (left) and 2000-shot average (middle) for a representative run. These images are unprocessed and were acquired using camera view 1 at a streamwise distance of x/H = 12 and at a fuel equivalence ratio of ϕ = 0.18. The laser sheet enters the test section from the left in the positive z-direction in the images presented, as though looking downstream from the given x/H plane. Fuel is injected in the center of the duct in the cross-stream direction and upstream of the image plane. The positive y-direction is towards the injector wall. Combustion occurs in semi-circular shaped regions of mixed fuel and air. Turbulence wrinkles the flame surface, as visible in the single-shot images. With a 2000-shot average, however, the OH distribution appears smooth. The lines left and right of the PLIF are scatter off of the test section windows and the above-mentioned filters were added to reduce this scatter; however, this scatter signal still exceeds the PLIF signal by as much as a factor of 15. Further analysis of the fully corrected images is discussed in the Results section.
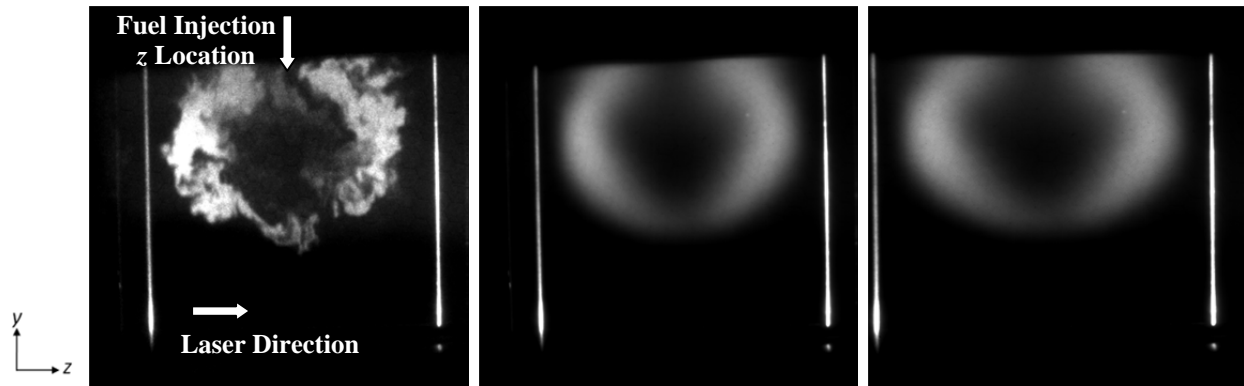
Fig. 5 Unprocessed single shot (left), raw 2000-shot average (middle), and unwarped 2000-shot average (right) PLIF images; $\phi = 0.18$, $x/H = 12$

To illustrate the unwarping process, Fig. 5 compares a raw (middle) and an unwarped (right) 2000-shot average PLIF image corresponding to camera view 1. Based on the laser scatter from the windows, it was apparent that even after the unwarping process a small rotation of 0.7 degrees (CCW) needed to be applied to the dataset. It is likely that the dotcard was slightly rotated with respect to the facility test section, causing the rotation error. In cases where the camera and optics were traversed downstream, there was a small shift of the PLIF signal and laser scatter of approximately 5 pixels over the entire scan range of camera view 1. This occurred because of a slight misalignment of the translation stage with respect to the facility. This shift was corrected in the final images.

As the dotcard image from camera view 2 contains unusable data beyond the edges of the cardstock, a smaller region on the dotcard which corresponds to the PLIF signal was selected and cropped. Both the cropped dotcard and PLIF images from camera view 2 were then stretched to match the spatial magnification used for camera view 1. Note that stretching does introduce some interpolation errors into the camera view 2 images. Prior to stretching, the spatial magnification in the y and z directions for camera view 2 were 11.97 pixels/mm and 6.87 pixels/mm, respectively. After stretching and unwarping of camera view 2, the effective spatial magnification for both camera views was 11.85 pixels/mm. The spatial resolution for camera views 1 and 2 was approximately 5 and 7 pixels, respectively.

After unwarping, the images were corrected for any spatial non-uniformity in the laser sheet using synchronized single-shot images of a Rhodamine dye cell captured from a Photometrics CoolSNAP interline CCD camera. To account for differences in the spatial resolution of PI-MAX2 and CoolSNAP images, a cardstock with a cutout pattern was placed into the laser sheet path, resulting in a pair of calibration images acquired from both cameras. These calibration images were used to properly align the sheet profiling images to the PLIF images. In addition to high frequency noise, repeatable small scale oscillations were observed in the sheet intensity profiles. These oscillations are likely a result of dust particles on the dye cell or irregularities in the glass material that contains the dye. Application of the unprocessed sheet correction profiles would result in non-physical streaks in the final PLIF data. Therefore, a Gaussian blur with an optimized sigma value of 25 pixels was applied to each sheet profile to eliminate any repeatable oscillations but still retain the overall profile. The blurred sheet profiles were then applied to the PLIF dataset on a shot-by-shot basis. This correction is significant, typically changing the PLIF signal intensity by a factor of 2 on one side of the image compared to the other. Also, it corrected for variations in laser intensity which could be as much as 50 percent during the test.
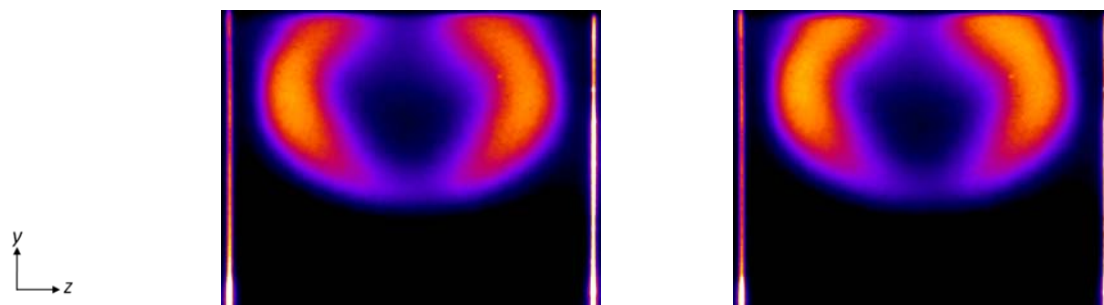

Fig. 6 Unwarped 2000-shot average before (left) and after (right) laser sheet correction; Camera view 1, $\phi = 0.18$, $x/H = 12$

Figure 6 shows an unwarped 2000-image average for ϕ = 0.18 and x/H = 12 before (left) and after (right) laser sheet correction. After the correction, there is a small but noticeable shift in the PLIF signal towards the injector wall. Further post processing (included in both images in Fig. 6) of the PLIF data included background subtraction using an average signal intensity over a region of negligible PLIF signal located near the combustor walls opposite of the injector. The images were then cropped to only include the interior region of the combustor. The laser scatter, however, was included in the images for reference. To account for two separate camera views, the average PLIF intensity from images using camera view 2 were corrected to match the average intensities in overlap regions that occur with camera view 1. A preset Fire color table available in ImageJ was applied to all images with consistent brightness and contrast values.

5 Results

Figure 7 shows a series of single-shot (left), average (center), and standard deviation (right) OH PLIF images for three different streamwise positions downstream of the injector plane. In these images, hydrogen fuel was injected at a global equivalence ratio of ϕ = 0.18. As can be seen from the average PLIF signal images, the overall size of the flame surface is relatively small near the fuel injector but then grows with increasing streamwise distance, and the OH concentration also increases. This is a combination of the accumulation of OH as it convects downstream as well as an increase in the reaction rate as the fuel and air become more mixed. Note that the color table is identical
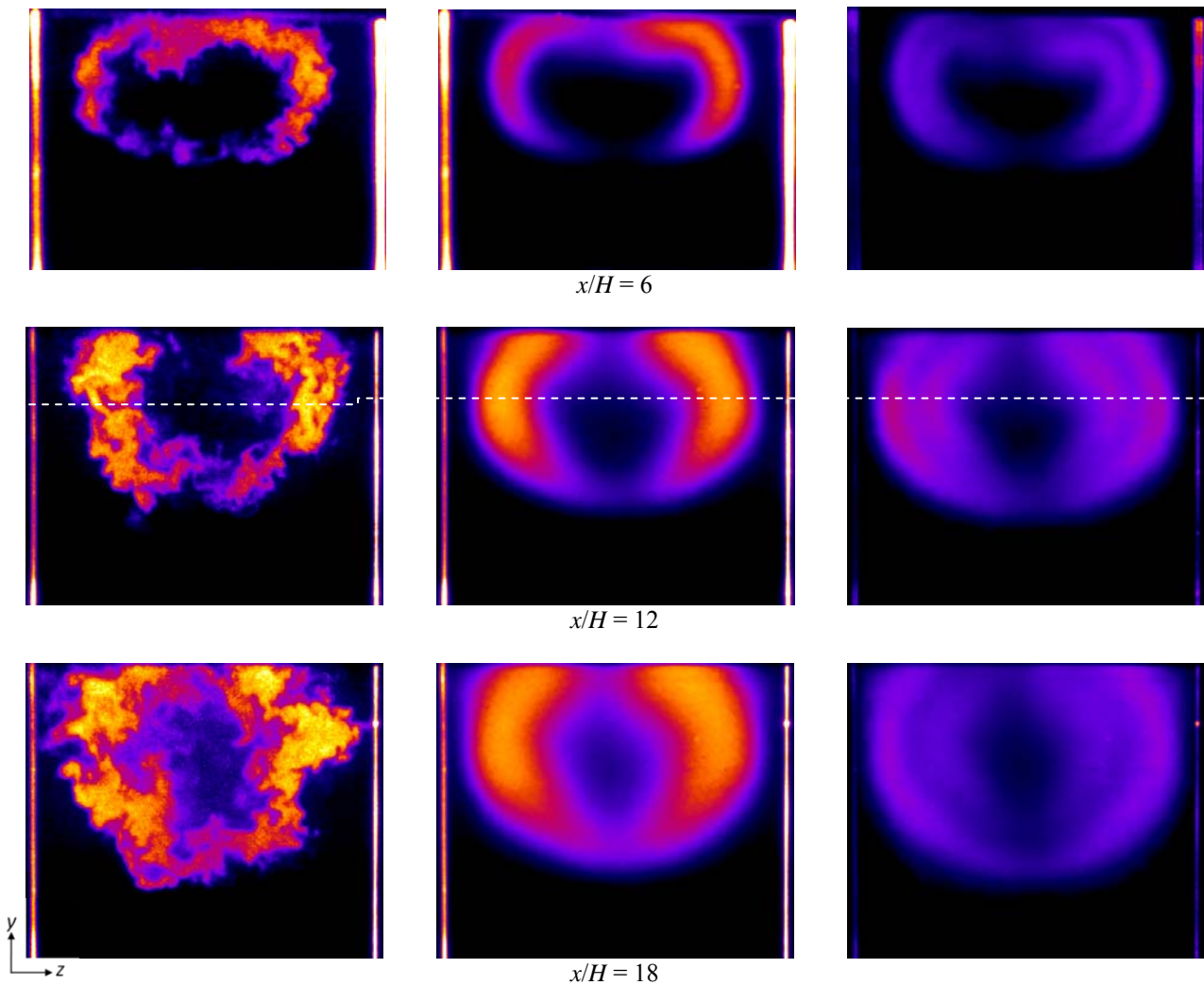

$x/H = 6$

$x/H = 12$

$x/H = 18$

Fig. 7 Single-shot (left), average (middle), and standard deviation (right) of the PLIF signal for three x/H positions indicated. ϕ = 0.18. Dashed line shows profile location for Fig. 8

for all of the images in the figure. The single shot images give an indication of the local length scales of turbulence near the reaction zone. The minimum size of turbulent structures observed, however, is limited by the camera resolution.
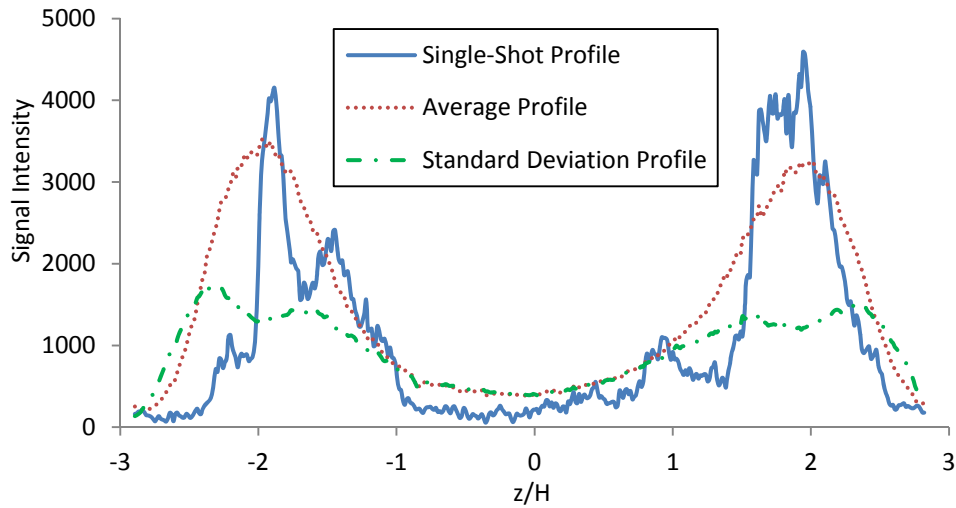

Fig. 8   Line plot of OH PLIF signal at an equivalent y/H position for single-shot, average, and standard deviation images for $x/H = 12$ and $\phi = 0.18$

The main source of turbulence production appears to be the shear layer that forms around the compression ramp. The shear layer interacts with the perimeter of the fuel jet, which enhances mixing and increases the rate of heat release. Interestingly, two distinct bands are visible in the standard deviation images. Each band indicates high levels of turbulence and regions where combustion occurs intermittently. The inner band coincides with the fuel-rich region while the outer band coincides with the fuel-lean region. The bands are more distinct near the fuel injector and become less pronounced with increasing streamwise distance. Again, this is likely due to more uniform mixing at planes further downstream. The bands are centered to either side of the peak levels in the mean signal images, as shown in Fig. 8. In this figure, a line plot through the center of the PLIF signal region is shown for the single shot, average, and standard deviation images from Fig. 7 for $x/H = 12$.

Figure 9 shows individual single-shot images for an equivalence ratio of $\phi = 0.18$ overlaid onto a 3D wireframe of the combustor. Selected x/H planes are shown from which the spreading rate of the jet and three dimensional distribution of the reaction zone can be visualized. Near the injector, combustion only occurs along the channel walls and along the shear layer that forms from the compression ramp sidewalls. The reaction does not initially occur along the jet perimeter near the high-speed core flow. However, at further downstream positions, combustion
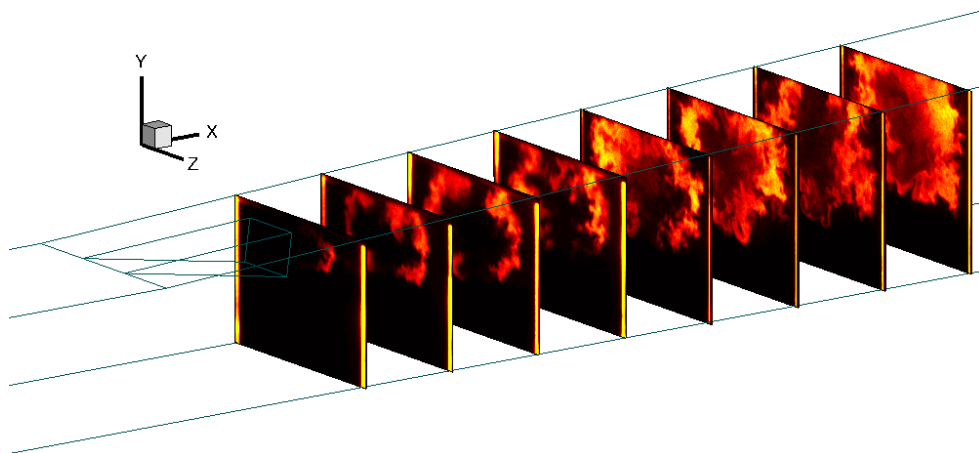

Fig. 9   Streamwise distribution of PLIF overlaid onto wireframe drawing of combustor. $\phi = 0.18$, scan from $x/H = 22$ to 1

occurs along all edges of the hydrogen jet. Similarly, Fig. 10 shows a 3D wireframe overlay for the higher fuel equivalence ratio case, $\phi = 0.36$, at equivalent x/H positions. Comparing Fig. 9 and Fig. 10, fluorescence is evidently greater for the higher fuel equivalence ratio; however, there is greater distribution of OH in the duct at the lower fuel equivalence ratio. This suggests that combustion is uniformly distributed more rapidly for lower fuel equivalence ratios.
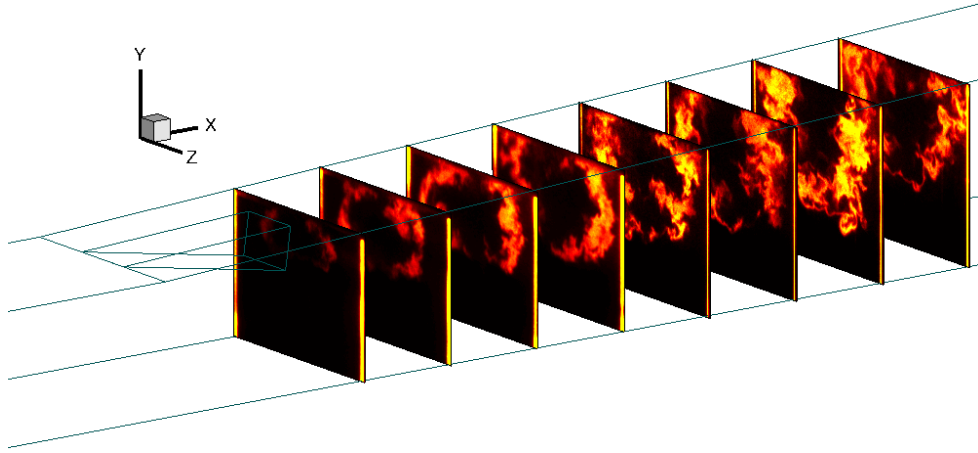

Fig. 10 Streamwise distribution of PLIF overlaid onto wireframe drawing of combustor for $\phi = 0.36$, scan from $x/H = 22$ to 1

A further effect of the fuel equivalence ratio on the distribution of OH is shown in Fig. 11, where the two values of ϕ were tested at an equivalent streamwise position. For a given mass flow rate of air, changes in the equivalence ratio are roughly proportional to changes in the concentration of OH. As expected, with a higher fuel flow rate case (left), higher concentrations of OH result in a brighter PLIF signal intensity. At this streamwise position ($x/H = 6$), asymmetry is clearly evident for $\phi = 0.18$ although some asymmetry is visible in the $\phi = 0.36$ case as well. At further downstream positions, both equivalence ratio tests show more symmetric distributions of OH.
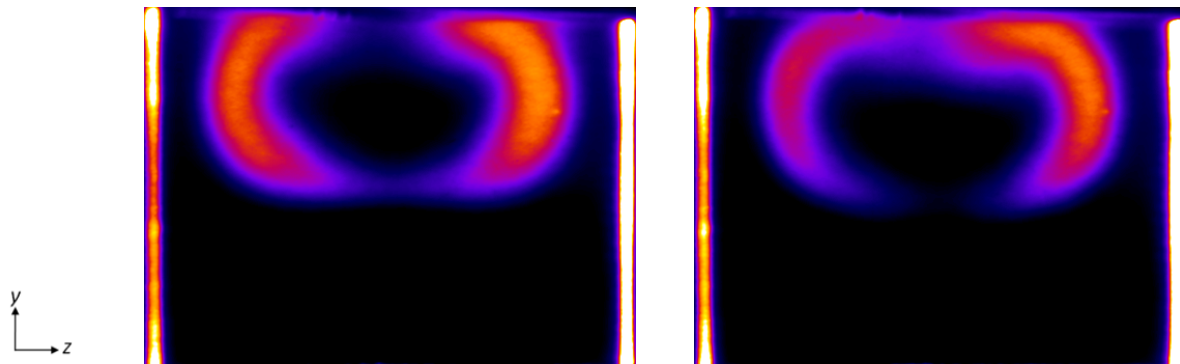

Fig. 11 Effect of equivalence ratio; $\phi = 0.36$ (left) and $\phi = 0.18$ (right) at $x/H = 6$; camera view 2

There are several mechanisms that can explain the asymmetry. It is possible that the flow diverges near the fuel injector creating a component of velocity in the direction of the laser sheet. If the laser was not spectrally centered on the $Q_1(8)$ transition, then a Doppler shift would cause an asymmetric PLIF distribution. However, based on the cross-stream velocity components predicted by Fulton et al. (2012), this effect is expected to be negligible. Another possible mechanism to explain the flow asymmetry is laser absorption. As the laser sheet transfers energy through the excitation of the hydroxyl radicals, the laser energy diminishes across the test section, resulting in a decrease of fluorescence across the image. Laser absorption effects can be corrected assuming Beer's law of absorption if the OH concentration distribution across the sheet is known. The direction of the laser sheet, however, is right-to-left in the image. The gradient in signal intensity is opposite to the laser direction, indicating that absorption is not a significant factor near the injector. However, laser sheet attenuation when combined with a related optical density effect known as radiative trapping could account for some of the asymmetry apparent in the image. Radiative

trapping is the reabsorption of fluorescence energy by the highly populated vibrational ground state of OH prior to reaching the imaging sensor. This results in a diminished signal reaching the sensor along longer detection paths through possibly higher concentrations of OH.

Flow asymmetry in the facility is another possible explanation for the PLIF asymmetry. In a previous study by Cutler et al. (2012), CARS measurements of the temperature distribution for the given configuration show significant temperature non-uniformities attributed to the heater, with higher temperatures recorded on the right side ($+z$ direction) of the facility upstream of the injector. It is possible that the asymmetric temperature distribution is one of the causes of the asymmetric PLIF signal distribution observed here.

Figure 12 shows a 3D iso-surface of the OH signal inset in the combustor wireframe using PLIF image stacks from camera views 1 and 2, covering the range $x/H = 0$ to 23.5 for the low fuel equivalence ratio, $\phi = 0.18$. The iso-level for the figure was set to 1500 counts, with an intensity scale identical to the results above, 100 to 5000, and the perspective is looking from the $+z$ side of the facility (equivalent side to the experimental PI-MAX2 camera images). Each image slice is generated from an average of 25 single-shot images to either side of the given image position, which smoothed the highly turbulent structures in the single-shot images but preserved the overall shape of the OH distribution. Qualitatively, the 3D PLIF distributions agree with OH concentration distributions predicted from numerical simulation (Fulton et al. 2012).
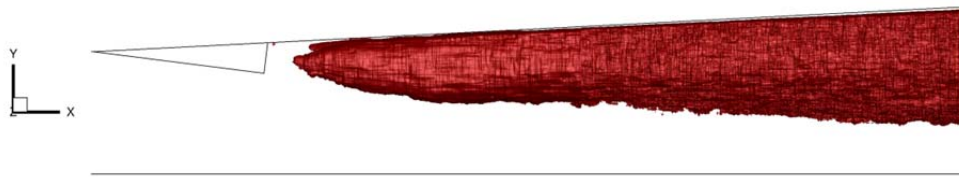

Fig. 12 3D iso-surface of OH PLIF signal using averaged images looking through the camera imaging wall; $\phi = 0.18$, $x/H = 0$ to 23.5, iso-level of 1500

Figure 13 shows the top view of the equivalent iso-surface in Fig. 12. While the signal intensities have been correlated at the overlap of the two camera views, the aforementioned asymmetry is apparent and is noticeably stronger for camera view 2, corresponding to the set of images nearest the injector. Similar results were found in a recent study for the combustor set up in configuration C (McRae et al. 2013). The asymmetry is attributed primarily to optical density effects (Quagliaroli et al. 1994). Since the camera is imaging in the opposite direction to the laser sheet, there can be significant contribution to asymmetry due to radiative trapping. This effect is further amplified in camera view 2, where the camera images the laser sheet pointed upstream through a larger concentration of OH compared to camera view 1. Laser sheet absorption similarly increases in magnitude with an increase in OH concentration and acts to cancel out the severity of asymmetry caused by radiative trapping. This may help to explain the weaker asymmetry in camera view 1, where the relative magnitudes of the two phenomena are much closer for downstream positions (increasing laser sheet absorption) and for imaging through lower OH concentrations (decreasing radiative trapping effects).
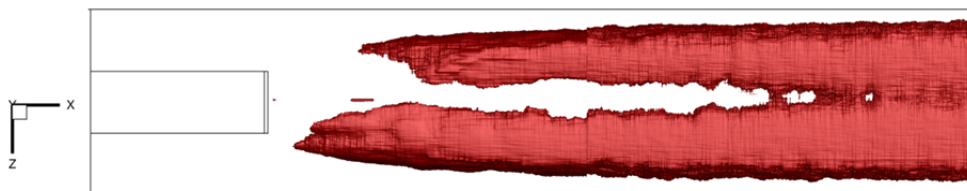

Fig. 13 3D iso-surface of OH PLIF signal with iso-level of 1500 looking through the diverging injector ramp wall; $\phi = 0.18$, $x/H = 0$ to 23.5

Inspecting the PLIF behavior at the injector face indicates possible recirculation upstream of the injector ramp. The distribution of PLIF signal at the injector ($x/H = 0$) is wider than the injector ramp itself and relatively strong signal is clearly visible up to $x/H = 0$, indicative of a potential recirculation zone on either side of the ramp. Figure 14 shows a stack of single shot images for the high fuel equivalence ratio. Arbitrary intensity scale and color maps were used to enhance details near the injector. PLIF signal upstream of the fuel injector nozzle is visible in the negative z-direction. Similar recirculation was observed for the low fuel equivalence ratio data, although the detected PLIF signal was weaker. Recirculation does not appear at positions below the bottom edge of the injector

surface. The signal was abruptly cut off at an angle in the negative *z*-direction due to the camera imaging angle respective to the imaged plane. In the positive *z*-direction, the injector ramp blocked the laser sheet at the given *y/H* position, and any OH occurring upstream of the fuel nozzle injector surface was not visible to the camera.
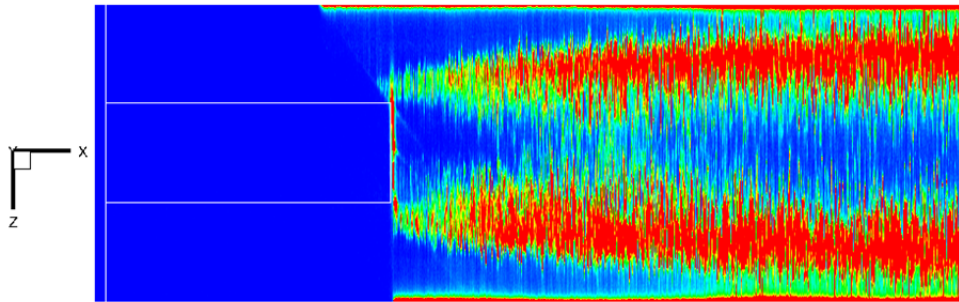

Fig. 14 Slice through a stack of single shot images at *y/H* = 2.0; ϕ = 0.36, *x/H* = -6 to 12

6 Conclusions

OH PLIF measurements in the combustor section of University of Virginia's dual-mode scramjet experiment have been performed. A detailed description of the post-processing, including the correction procedure for optical distortions, has been discussed. Visualization of the turbulent reaction zones corresponding to two equivalence ratio tests was achieved. Large scale turbulence structures are visible along the entire flame surface. Standard deviation plots reveal two bands indicating large fluctuation levels near the fuel-rich jet interior and near the fuel-lean jet exterior. Asymmetry near the fuel injector was observed for the lower equivalence ratio tests. Flow asymmetry due to non-uniform temperature distribution in the facility and optical density effects due to radiative trapping and laser sheet attenuation are the likely causes of this phenomenon. Indication of recirculation upstream of the fuel injector ramp was observed for both fuel equivalence ratios. The results reported here serve as a dataset for numerical model assessment.

References

Busa KM, Bryner E, McDaniel JC, Goyne CP, Smith CT, Diskin GS (2011) Demonstration of Capability of Water Flux Measurement in a Scramjet Combustor using Tunable Diode Laser Absorption Tomography and Stereoscopic PIV. 49th AIAA Aerosp Sci Meet Exhib. doi: 10.2514/6.2011-1294

Curran ET (2001) Scramjet Engines: The First Forty Years. J Propuls Power 17:6:1138-1148. doi: 10.2514/2.5875

Cutler AD, Magnotti G, Cantu L, Gallo E, Danehy PM, Rockwell R, Goyne C, McDaniel J (2012) Dual-Pump CARS Measurements in the University of Virginia's Dual-Mode Scramjet: Configuration A. 50th AIAA Aerosp Sci Meet Exhib. doi: 10.2514/6.2013-335

Danehy PM, Alderfer DW, Inman JA, Berger KT, Buck GM, Schwartz RJ (2008) Fluorescence Imaging and Streamline Visualization of Hypersonic Flow over Rapid Prototype Wind-Tunnel Models. Proc IMechE, Part G: J Aerosp Eng 222(G5): 637-651. doi: 10.1243/09544100JAERO295

Forescue P, Stark J (1995) Spacecraft System Engineering. Wiley, New York

Fry RS (2004) A Century of Ramjet Propulsion Technology. J Propuls Power 20:1:27-58. doi: 10.2514/1.9178

Fulton JA, Edwards JR, Hassan HA, Rockwell R, Goyne C, McDaniel J, Smith C, Cutler A, Johansen C, Danehy PM, Kouchi T (2012) Large-Eddy / Reynolds-Averaged Navier-Stokes Simulations of a Dual-Mode Scramjet Combustor. 50th AIAA Aerosp Sci Meet Exhib

Goldstein CS, Schultz IA, Jeffries JB, Hanson RK (2011) Tunable Diode Laser Absorption Sensor for Measurements of Temperature and Water Concentration in Supersonic Flows. 49th AIAA Aerosp Sci Meet Exhib

Goyne CP, Rodriguez CG, Krauss RH, McDaniel JC, McClinton CR (2006) Experimental and Numerical Study of a Dual-Mode Scramjet Combustor. J Propuls Power 22:3:481-489. doi: 10.2514/1.13215

Hank J, Murphy J, Mutzman R (2008) The X-51A Scramjet Engine Flight Demonstration Program. 15th AIAA Int Space Planes and Hypersonic Syst Technol Conf. doi: 10.2514/6.2008-2540

Heiser WH, Pratt DT (1994) Hypersonic Airbreathing Propulsion. American Institute of Aeronautics and Astronautics, Inc., Washington, DC

Johansen CT, McRae CD, Danehy PM, Gallo E, Cantu L, Magnotti G, Cutler A, Rockwell R, Goyne C, McDaniel J (2012) OH PLIF Visualization of the UVa Supersonic Combustion Experiment: Configuration A. 28th AIAA Aerodyn Meas Technol Ground Test Flight Test Conf. doi: 10.2514/6.2012-2887

McRae CD, Johansen CT, Danehy PM, Gallo E, Cantu L, Magnotti G, Cutler A, Rockwell R, Goyne C, McDaniel J (2013) OH PLIF Visualization of the UVa Supersonic Combustion Experiment: Configuration C. 51st AIAA Aerosp Sci Meet. doi: 10.2514/6.2013-34

O'Byrne S, Stotz I, Neely AJ, Boyce RR, Mudford NR, Houwing AFP (2005) OH PLIF Imaging of Supersonic Combustion using Cavity Injection. 13th AIAA/CIRA Int Space Planes and Hypersonics Syst Technol Meet. doi: 10.2514/6.2005-3357

Quagliaroli TM, Laufer G, Hollo SD, Krauss RH, Whitehurst RB, McDaniel JC (1994) Planar KrF Laser-Induced OH Fluorescence Imaging in a Supersonic Combustion Tunnel. J Propuls Power 10:3:377-381. doi: 10.2514/3.23767

Rasband WS (1997-2009) ImageJ. US Natl Inst Health, Bethesda, MD, USA. http://rsb.info.nih.gov/ij

Rockwell RD, Goyne CP, Rice BE, Tatman BJ, Smith C, Kouchi T, McDaniel JC, Fulton JA, Edwards JR (2012) Close-Collaborative Experimental and Computational Study of a Dual-Mode Scramjet Combustor. 50th AIAA Aerosp Sci Meet Exhib

Smart M (2009) HiFiRE 7 – Development of a 3-D Scramjet for Flight Testing. 16th AIAA/DLR/DGLR Int Space Planes and Hypersonic Syst Technol Conf. doi: 10.2514/6.2009-7259

Smart MK, Hass NE, Paull A (2006) Flight data analysis of the HyShot 2 scramjet flight experiment. AIAA J 44:10:2366-2375. doi: 10.2514/1.20661

Sorzano COS, Thevenaz P, Unser M (2005) Elastic Registration of Biological Images Using Vector-Spline Regularization. IEEE Trans Biomed Eng 52:4:652-663. doi: 10.1109/TBME.2005.844030

Tetlow MR, Doolan CJ (2007) Comparison of Hydrogen and Hydrocarbon-Fueled Scramjet Engines for Orbital Insertion. J Spacecr Rockets 44:2:365-373. doi: 10.2514/1.24739

Voland RT, Huebner LD, McClinton CR (2006) X-43A Hypersonic Vehicle Technology Development. Acta Astronautica 59:181-191. doi: 10.1016/j.actaastro.2006.02.021